PAPER

Interior x-ray diffraction tomography with low-resolution exterior information
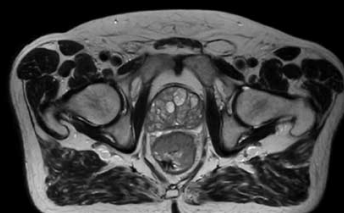
Physics in Medicine & Biology

IPEM Institute of Physics and Engineering in Medicine

PAPER

Interior x-ray diffraction tomography with low-resolution exterior information

Zheyuan Zhu[1,3], Alexander Katsevich[2] and Shuo Pang[1]

[1] CREOL, The College of Optics and Photonics, University of Central Florida, Orlando, FL 32816, United States of America
[2] Department of Mathematics, University of Central Florida, Orlando, FL 32816, United States of America
[3] Author to whom any correspondence should be addressed.

E-mail: zyzhu@knights.ucf.edu

Abstract

X-ray diffraction tomography (XDT) resolves spatially-variant XRD profiles within macroscopic objects, and provides improved material contrast compared to the conventional transmission-based computed tomography (CT). However, due to the small diffraction cross-section, XDT suffers from long imaging acquisition time, which could take tens of hours for a full scan using a table-top x-ray tube. In medical and industrial imaging applications, oftentimes only the XRD measurement within a region-of-interest (ROI) is required, which, together with the demand to reduce imaging time and radiation dose to the sample, motivates the development of interior XDT systems that scan and reconstruct only an internal region within the sample. The interior problem does not have a unique solution, and a direct inversion on the truncated projection data often leads to large reconstruction errors in ROI. To reduce the truncation artifacts, conventional attenuation-based interior reconstruction problems rely on a known region or piecewise constant constraint within the ROI. Here we propose a quasi-interior XDT scheme that incorporates a small fraction of projection information from the exterior region to assist ROI reconstruction. In the phantom simulation, a small amount (17% of exterior region) of added exterior projection data improves the reconstruction quality by ~50%. The addition of exterior samplings in the experiment demonstrates improved spatial and XRD profile reconstructions compared to total-variation-based reconstruction or sinogram extrapolation. We expect our quasi-interior XDT to obviate the requirement on prior knowledge of the object or its support, and to allow the ROI reconstruction to be performed with the fast, widely-used filtered back-projection algorithm for easy integration into real-time XDT imaging modules.

1. Introduction

X-ray diffraction (XRD) is a material-specific probe at molecular level. Due to the high penetration depth of x-ray beam, XRD is especially suitable for analyzing thick samples in applications including solving the crystalline structure (Schroer *et al* 2006, Schaff *et al* 2015), detecting low-concentration chemical substances (Bleuet *et al* 2008, Valentini *et al* 2011, Sottmann *et al* 2017), and more recently, diagnosis of structural defects in bones, prosthetic implants (Stock *et al* 2008, Mochales *et al* 2011), or disease-related anomaly in soft tissues (He *et al* 2017, Moss *et al* 2017). For heterogeneous object on the centimeter scale or larger, resolving the XRD profile of individual sample voxels requires a combination of XRD measurement and computed tomography (CT) (Harding *et al* 1987), which captures the XRD signals under different projections and is termed x-ray diffraction tomography (XDT). However, because of the weak XRD signal, XDT scan is typically conducted with a high-brilliance synchrotron source (Kleuker *et al* 1998, Schroer *et al* 2006, Bleuet *et al* 2008, Stock *et al* 2008, Jensen *et al* 2011), which hinders its adoption in industrial and medical applications. A number of XDT systems based on x-ray tubes have been demonstrated using collimators on either the source side or detector side (Westmore *et al* 1997, Delfs and Schlomka 2006, Harding 2009), but a full scan on an object of ~20 mm in diameter involves tens of hours of imaging time, and delivers a high radiation dose to the sample.

Figure 1. Geometry of pencil-beam XDT. The red, dashed circle marks the ROI.
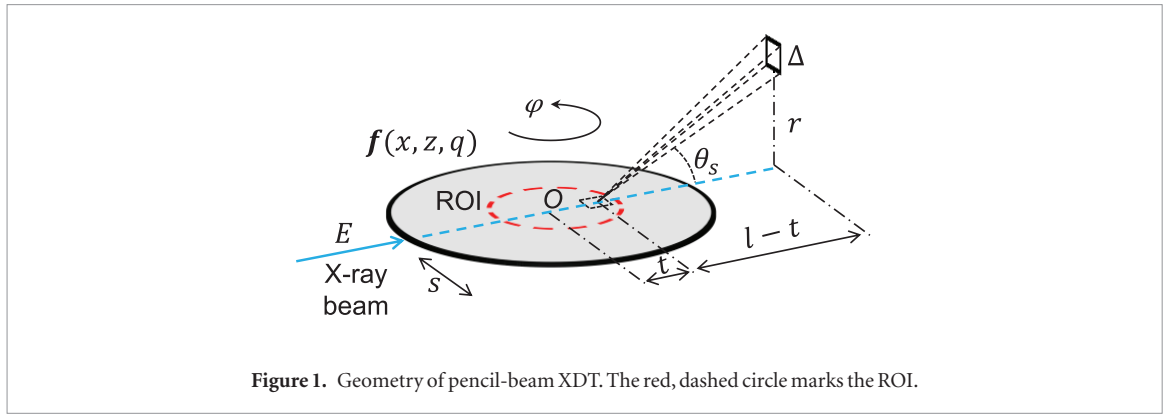
In biomedical studies or industrial inspections, XDT is ideal for a secondary scan, in which only the material composition within an ROI is desired (Harding and Schreiber 1999, Harding 2004). For these applications, interior XDT limits the projection measurement to the ROI region to reduce the imaging time and excessive radiation dose outside ROI, and provides comparable material specificity as a full XDT scan (Zhu *et al* 2018). Similar to the interior problem in CT, interior XDT also requires prior knowledge about the object, either in the form of a known sub-region (Kudo *et al* 2007, Jin *et al* 2012) or piecewise constant constraint (Wang and Yu 2009, Yang *et al* 2010), to stabilize the ROI reconstruction. However, knowing the *in situ* XRD profile of a small region within the whole sample is not possible in XDT. Piecewise constant constraint could be a feasible prior for interior XDT, yet it is not generally applicable to samples with fine features or with a high scattering density gradient. Based on the non-localized filtered back-projection used in XDT reconstruction, here we introduce a small fraction of projection measurement in the exterior region to stabilize the ROI reconstruction. The combined interior and exterior information provides an alternative approach to the existing interior reconstruction techniques that require prior knowledge of the sample.

2. Theory

2.1. X-ray diffraction tomography (XDT)

The pencil-beam XDT system (figure 1) illuminates the sample with a collimated, narrow-band x-ray beam. Upon interacting with the sample, the scattering mechanism of x-ray photons falls into two major categories, Compton incoherent scattering and Rayleigh coherent scattering. In coherent scattering, scattered photons maintain the same energy but are deflected towards a different direction away from the incident direction. Under small scattering angles, coherent scattering is the dominant scattering process (Johns and Yaffe 1983) that gives rise to the XRD signature of the material. The number of diffracted photons dI in the direction θ_s from a volume dV is determined by the scattering geometry and molecular form factor

$$dI = I_0 \frac{r_e^2}{2} (1 + cos^2\theta_s) f(\mathbf{r}, q) \mathrm{d}\Omega \mathrm{d}V \mathrm{d}q, \tag{1}$$

where I_0 is the intensity of the incident beam; θ_s is the angle between incident and scattered radiation, and $\cos\theta_s \approx 1$ for small angles; $d\Omega = \Delta^2/(r^2 + (l-t)^2)$ is the solid angle covered by the detector pixel with size Δ located at distance r away from the pencil beam, and l is the distance between the rotation center and detector plane. The scattering volume $dV = Adt$, where A is the cross-section area of the pencil beam; t is the depth of scatter along the pencil beam. $f(x, z, q) = n(x, z) F^2(x, z, q)$ is the product between the density of the scatter $n(x, z)$ and the molecular form factor $F(x, z, q)$. The momentum transfer q that causes the deflection of photons with energy E and scattering angle θ_s is defined by the Bragg's law

$$q = E/hc \, \sin(\theta_s/2), \tag{2}$$

where h and c represent Plank's constant and speed of light, respectively; E is the energy of the incident x-ray.

We can introduce a series of first-order approximations to equation (2) that relates XDT to a volumetric tomography reconstruction problem (Zhu *et al* 2018). At small diffraction angles, $\sin(\theta_s/2) \approx r/(2(l-t))$. Given that the distance from the rotation center to the detector, l, is much larger than the size of the sample, the Taylor expansion on the $1/(l-t)$ terms around $t = 0$ simplifies the Bragg's law in equation (2) to

$$q = \frac{Er}{2hcl}\left(1 + \frac{t}{l}\right). \tag{3}$$

Equation (3) describes the momentum transfer probed by the detector pixel located at a distance r away from the pencil beam. The intensity on the detector is a multiplexed measurement of the XRD signals along the pencil
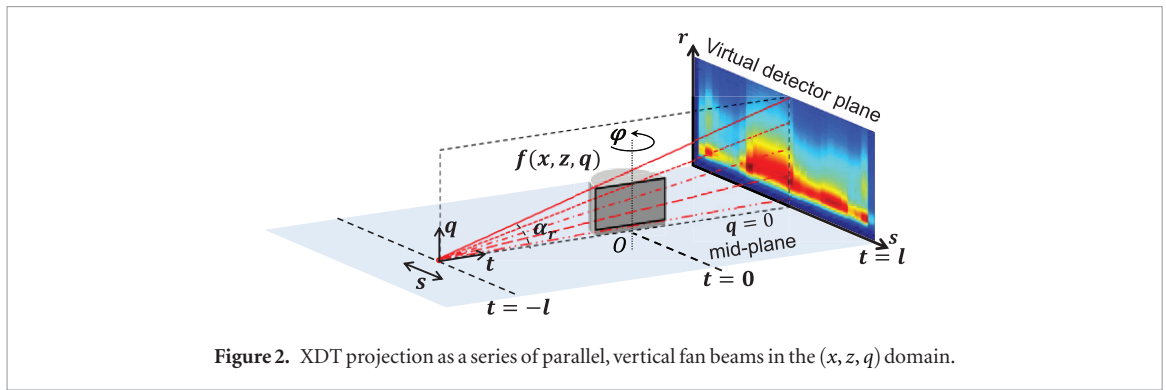
Figure 2. XDT projection as a series of parallel, vertical fan beams in the (x, z, q) domain.

beam. To resolve the complete object function, $f(x, z, q)$, the sample needs to be translated across the beam by the distance s in the (x, z) plane, and rotated around the vertical axis by the angle ϕ similarly to that in a pencil-beam CT. The total number of photons collected by a detector pixel under sample offset s and projection angle ϕ is

$$I(r, s)_\phi = Cw(r) \int_\Gamma f(s\hat{\Theta} + t\hat{\Theta}^\perp + \tan \alpha_r \left(1 + \frac{t}{l}\right) \hat{q}) \mathrm{d}t, \tag{4}$$

where $C = I_0 A r_e^2$ is a constant proportional to the source intensity; $\hat{\Theta} = (\cos\phi, \sin\phi, 0)$ and $\hat{\Theta}^\perp = (-\sin\phi, \cos\phi, 0)$ are the directional vectors parallel and perpendicular to the incident x-ray beam in the x-z plane, respectively; $\hat{q} = (0, 0, 1)$ is the unit vector along the momentum transfer dimension; $w(r) = \Delta^2/(r^2 + l^2)$ is a weight to account for the decay of the scattering signal.

2.2. Interior XDT reconstructions

Equation (4) implies that the integral is performed along the line Γ in the (x, z, q) domain with slope $\tan \alpha_r = Er/(2hcl)$, where α_r is the angle with respect to the mid-plane ($q = 0$). Figure 2 illustrates a family of XDT projection lines with r as a parameter, which, combined with sample translation, form a series of parallel, vertical fan-beam projections of the object $f(x, z, q)$ onto the virtual detector plane $(s, r)_\phi$ at rotation angle ϕ. The XDT reconstruction follows a filtered back-projection modified from the Feldkamp–Davis–Kress algorithm (Feldkamp *et al* 1984) (modified-FDK, for short), in which the back-projection is performed along diverging lines in the z-q plane, and parallel lines in the x-z plane.

2.2.1. Addition of low-resolution exterior projections

Let $a_1(\phi)$, $a_2(\phi)$ denote the two ends of the object support at each projection angle, such that $I(r, s)_\phi = 0$ if $s < a_1(\phi)$ or $s > a_2(\phi)$. Let $b_1(\phi), b_2(\phi)$ denote the boundary of ROI region, within which the pencil-beam scan is performed at each projection angle. For interior XDT scan, equation (4) becomes

$$I(r, s)_\phi = Cw(r) \int_{t=a_1(\phi)}^{a_2(\phi)} f(s\hat{\Theta} + t\hat{\Theta}^\perp + \tan \alpha_r \left(1 + \frac{t}{l}\right) \hat{q}) dt, \quad b_1(\phi) \leqslant s \leqslant b_2(\phi), \tag{5}$$

which indicates that interior XDT detects the same range of scattering angles and the number of projections as a conventional pencil-beam XDT, except that only the ROI region of the sample is scanned. Analogous to the conversion between fan-beam CT and parallel-beam CT (Lavrov and Simonov 2010), the projection lines in the parallel fan-beam geometry can be rearranged to a half-cone-beam projection of (x, z, q) onto the virtual detector plane $(s, r)_\phi$ at each projection angle. Therefore interior XDT is equivalent to a transversely-truncated cone-beam CT. Inspired by the truncated cone-beam CT reconstruction frameworks (Van Gompel *et al* 2004, Xiao *et al* 2007), which combine LR full field-of-view (FOV) scans with high magnification, ROI-only projections, our quasi-interior XDT introduces additional LR measurements of the exterior region, and linearly interpolate the missing pixels between two adjacent LR samplings to form a complete sinogram with homogenous resolution in both ROI and exterior region. The modified-FDK then back projects the complete sinogram $I(r, s)_\phi$ to the object domain (x, z, q) to reconstruct the full FOV, from which only the ROI region is extracted. As a comparison with existing interior reconstruction techniques used in conventional CT, we also reconstructed the ROI from truncated projection data with sinogram extrapolation and iterative total-variation regularization (IR-TV for short), which are detailed in sections 2.2.2 and 2.2.3, respectively.

2.2.2. Extrapolation on truncated ROI projection

In the filtered back-projection framework, the ROI reconstruction from truncated projection data does not have a unique solution, since any exterior data, combined with the interior projection, can be inversed by modified-FDK. Based on the continuity of the projection data associated with a realistic sample, it is possible to supplement

the missing exterior projection via a continuous extrapolation on the truncated projection from ROI boundary to the object support (Van Gompel *et al* 2006). Specifically, we extrapolate the measured interior sinogram into the exterior region via

$$I(r,s)_\phi = \begin{cases} c_1\sqrt{s - a_1(\phi)}, & s < b_1(\phi) \\ c_2\sqrt{a_2(\phi) - s}, & s > b_2(\phi) \end{cases}, \tag{6}$$

where c_1, c_2 are constants that ensures continuity across the ROI boundary, and are calculated according to

$$\begin{cases} c_1 = \frac{I(r,b_1(\phi))_\phi}{\sqrt{b_1(\phi) - a_1(\phi)}} \\ c_2 = \frac{I(r,b_2(\phi))_\phi}{\sqrt{a_2(\phi) - b_2(\phi)}} \end{cases}. \tag{7}$$

2.2.3. Total-variation (TV) regularization

In addition to the filtered back-projection–based frameworks, iterative reconstruction that incorporates total variation (TV) regularization (IR-TV) to enforce the piecewise constant constraint is also widely used in interior problem. In the iterative reconstruction algorithm, both object $\mathbf{f}$ and measurement $\mathbf{I}$ are discretized. The system matrix $\mathbf{H}$ relating $\mathbf{f}$ and $\mathbf{I}$ is constructed from the pixels hit by each beam and the weight $w(r)$ in equation (4). Each pencil-beam measurement is an independent entry in the system matrix $\mathbf{H}$ in IR-TV. For interior measurement, we limit the size of the matrix $\mathbf{H}$ to cover only the pencil beams passing through ROI region.

IR-TV is an optimization problem that minimizes the objective function in equation (8), which consists of a Poisson likelihood $P(\mathbf{I}|\mathbf{f})$ of observing the measurement $\mathbf{I}$ given the object $\mathbf{f}$, and a TV regularizer

$$\widehat{\mathbf{f}} = \arg\min_{\mathbf{f}'} \left\{ -\log P\left(\mathbf{I}|\mathbf{f}'\right) + \tau \mathrm{TV}\left(\mathbf{f}'\right) \right\}, \tag{8}$$

where the TV operator is defined as

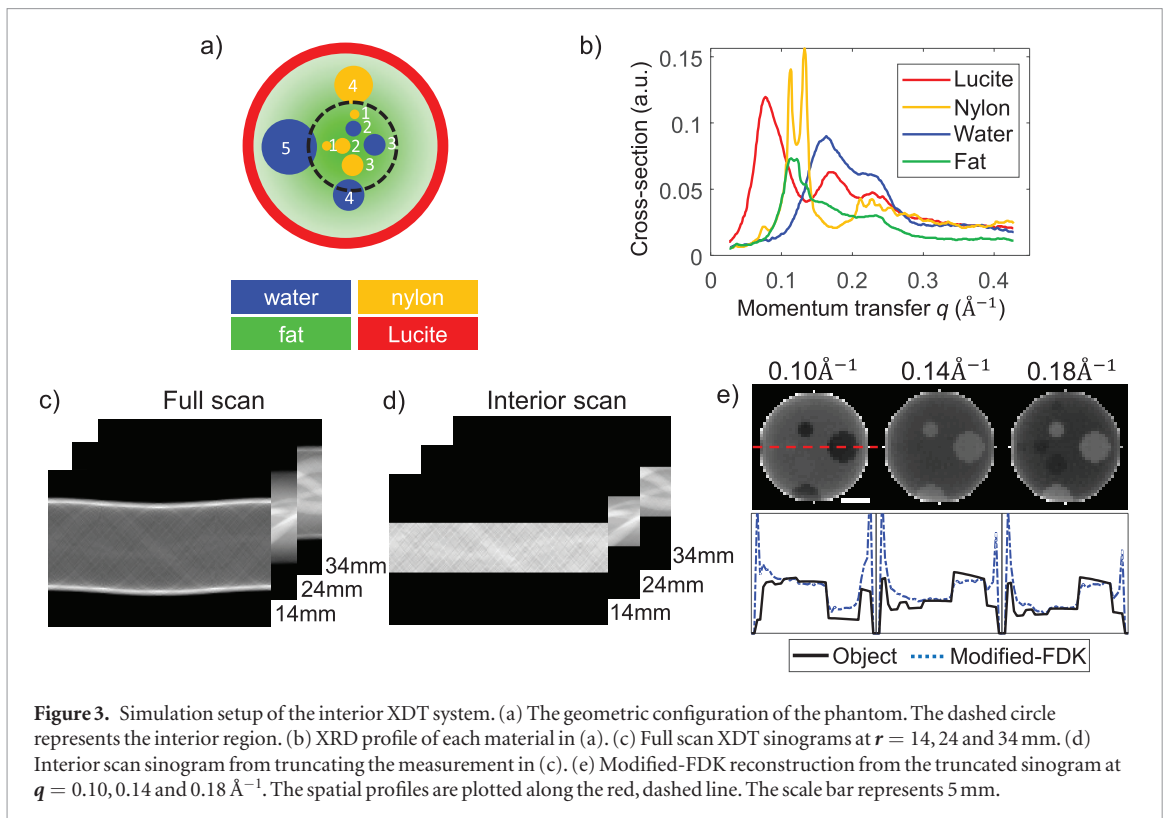$$\mathrm{TV}(\mathbf{f}) = \sum_{i,j,k} \sqrt{(f_{i+1,j,k} - f_{i,j,k})^2 + (f_{i,j+1,k} - f_{i,j,k})^2} \tag{9}$$

in which the index i and j represents the spatial dimension x and z, respectively. k represents the index in the momentum transfer domain. The optimization was implemented by an EM algorithm (Moon 1996) embedded with TV regularization (Chambolle 2004) in each iteration. The iteration terminates when the relative change in the objective function (equation (8)) is smaller than 10^{-4}. The parameter τ that yields the minimal objective function at the end of the iterations is selected.

3. Materials and methods

3.1. Simulation setup

A numerical phantom was designed to evaluate the performance of our quasi-interior XDT reconstruction based on the modified-FDK, and compare it with existing interior reconstruction methods. Figure 3(a) shows the geometric configuration of the phantom, which consists of circular regions of five different diameters, marked by the digit next to each circle. The smallest to the largest diameters are 0.8, 1.4, 1.8, 2.6 and 3.2 mm, respectively. Each region is filled with either water or Nylon, and wrapped in an 18 mm-diameter Lucite tube. The tube is filled with saturated fat, whose density, $n(x,z)$, follows a Gaussian function along the radial direction. XRD profiles (figure 3(b)) reported in the previous works (Harding *et al* 1987, Kidane *et al* 1999) were assigned to each material region in the phantom. The 10 mm-diameter dashed circle in (a) marks the ROI, within which the sampling interval is 0.25 mm. The sampling interval outside ROI is 1.25 mm. Without losing generality, we coincide the center of both the Lucite tube and ROI with the rotation center, so that a_1, a_2, b_1 and b_2 are all independent on ϕ. The 180° projections were uniformly covered at 1° step size. The full field-of-view XDT measurements were generated by the system matrix $\mathbf{H}$ constructed from the distance-driven projection geometry (Siddon 1985). For IR-TV reconstruction, we additionally constructed a system matrix $\mathbf{H}_2$ that linked the object to its interior measurements. Figure 3(c) shows the sinogram $I(s,\phi)_r$ at $r = 10, 20$ and 30 mm of the full XDT scan. The interior scan (d) was simulated by extracting the ROI projection from the full scan in (c). Figure 3(e) shows the modified-FDK reconstruction from truncated sinograms, in which the artifacts on the ROI boundary are clearly visible (Natterer 1986, Wang and Yu 2013). The reconstruction quality is assessed by the normalized mean square error (NMSE), which is defined as $\mathrm{NMSE} = \left\|\widehat{\mathbf{f}}_{\mathrm{ROI}} - \mathbf{f}_{0,\mathrm{ROI}}\right\|^2 / \left\|\mathbf{f}_{0,\mathrm{ROI}}\right\|^2$, where $\widehat{\mathbf{f}}_{\mathrm{ROI}}$ represents the reconstruction within ROI region, $\mathbf{f}_{0,\mathrm{ROI}}$ is the ground truth of the object in the ROI, and $\|\cdot\|$ denotes the L2-norm.

Figure 3. Simulation setup of the interior XDT system. (a) The geometric configuration of the phantom. The dashed circle represents the interior region. (b) XRD profile of each material in (a). (c) Full scan XDT sinograms at $r = 14, 24$ and 34 mm. (d) Interior scan sinogram from truncating the measurement in (c). (e) Modified-FDK reconstruction from the truncated sinogram at $q = 0.10, 0.14$ and 0.18 Å^{-1}. The spatial profiles are plotted along the red, dashed line. The scale bar represents 5 mm.
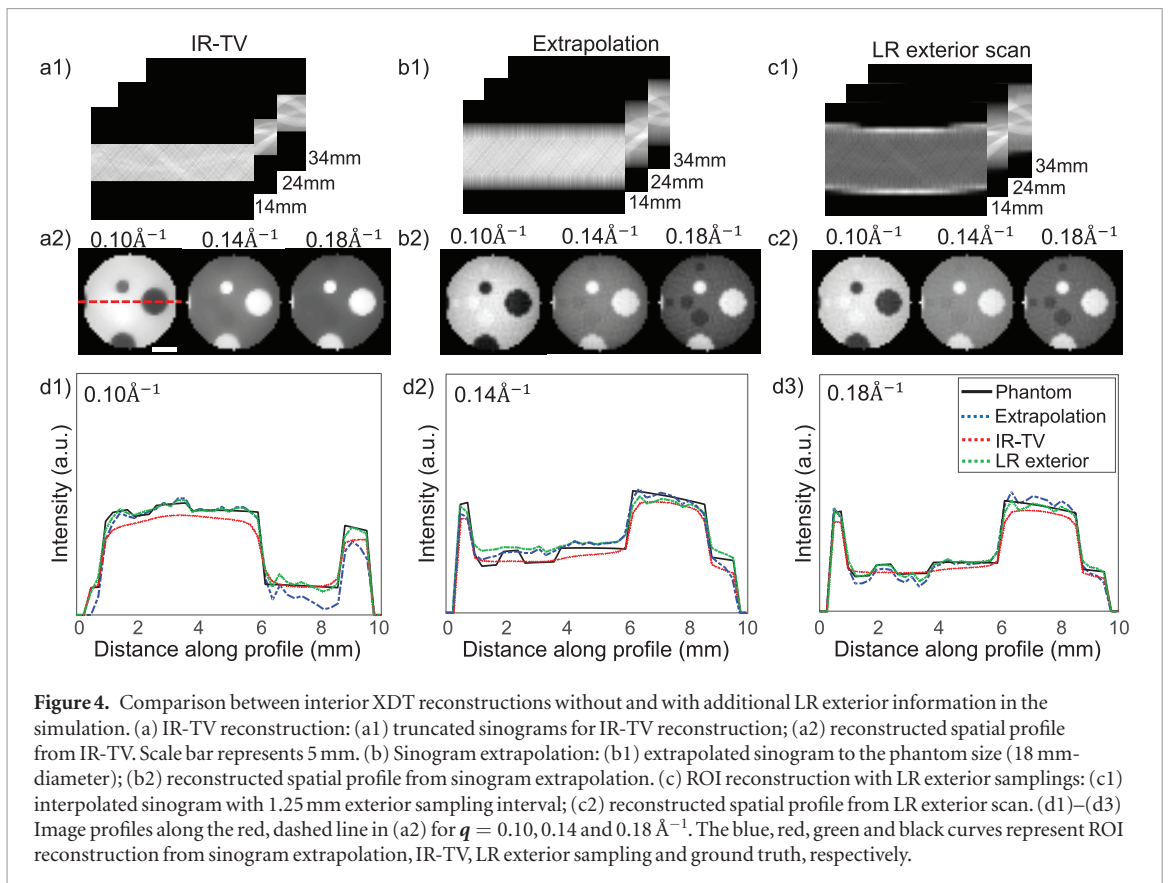
3.2. Experiment setup

The experiment employed a copper-anode x-ray tube (XRT60, Proto Manufacturing) operating at 45 kV and 40 mA, which emits a characteristic spectrum peak at 8 keV. A pair of lead pinholes collimated the beam to a diameter of 2 mm. The sample was mounted on a rotational stage (RV1200P, Newport) to cover 180° projection angles with 3.6° step size. The sample consisted of three cylindrical vials filled with water, soybean oil and ethanol, and was wrapped inside a 27 mm-diamter, 1 mm-thick Teflon tube. A circular region (11 mm in diameter) at the center of the sample was marked as the ROI. The sample was translated by a linear stage (UTM150CC, Newport) across the pencil beam with step size of 1 mm inside the ROI, and 5 mm outside the ROI. The diffracted x-ray was captured by a flat panel detector (1215CF-MP, Rayence) located at 120 mm away from the sample. The detector pixel size is 0.2 mm under 4× binning model. We performed an azimuthal binning within a series of concentric, 2-pixel-wide rings to reduce each 2D image to 1D intensity profile along the radial direction. The central 10 mm × 10 mm region on the detector was covered by a lead beam stop to block the transmitted beam. The acquisition time for each diffraction pattern was 30 s. The total imaging time of 15 XRD patterns, 11 in the ROI and 4 in the exterior region, under 50 projections was ~6.5 h. This included the integration time and the ~1 s motion and data transfer time between two pencil beam measurements. To measure the single-point XRD reference, the 2 mm-wide tip of each vial was scanned by the pencil beam to collect 6 XRD profiles for water, oil and ethanol. A CT scan of the whole sample with 0.1 mm spatial resolution under 180° projections at 1° step size was also performed.

3.3. Material classification

The material classification based on the reconstructed XRD profiles was performed using support vector machines (SVM) (Cortes and Vapnik 1995) with Gaussian kernel. The discrete XRD profile $f(q)$ associated with each pixel (x, z) was treated as a high-dimensional vector $\mathbf{f} = \{f_{q1}, f_{q2}, \ldots, f_{qn}\}$. Given a set of training examples (XRD profiles) and their associated classes (material category), SVM draws optimal hyper-surfaces to discriminate high-dimensional XRD profiles into one of the 4 classes (ethanol, water, oil and background). The training set for each material was obtained from the six reference XRD measurements. To separate the background from three material classes, six randomly-sampled pixels in the gap among the vials on the reconstructed phantom were also included in the training set. In total, four binary SVMs were constructed to discriminate one class (either a material or the background) against the rests. Each SVM output a score $y(\mathbf{f}) = \sum_i \alpha_i y_i k(\mathbf{f}_i, \mathbf{f}) + b_i$, where y_i is the binary label of the training vector $\mathbf{f}_i$; α_i and b_i are sets of trained SVM parameters; and $k(\mathbf{u}, \mathbf{v}) = \exp(-\|\mathbf{u} - \mathbf{v}\|^2 / (2\sigma^2))$ represents the Gaussian kernel (with scale σ) applied to the Euclidean distance between two vectors. The class that yields the highest score determines the material of each ROI pixel.

Figure 4. Comparison between interior XDT reconstructions without and with additional LR exterior information in the simulation. (a) IR-TV reconstruction: (a1) truncated sinograms for IR-TV reconstruction; (a2) reconstructed spatial profile from IR-TV. Scale bar represents 5 mm. (b) Sinogram extrapolation: (b1) extrapolated sinogram to the phantom size (18 mm-diameter); (b2) reconstructed spatial profile from sinogram extrapolation. (c) ROI reconstruction with LR exterior samplings: (c1) interpolated sinogram with 1.25 mm exterior sampling interval; (c2) reconstructed spatial profile from LR exterior scan. (d1)–(d3) Image profiles along the red, dashed line in (a2) for $q = 0.10, 0.14$ and 0.18 Å^{-1}. The blue, red, green and black curves represent ROI reconstruction from sinogram extrapolation, IR-TV, LR exterior sampling and ground truth, respectively.
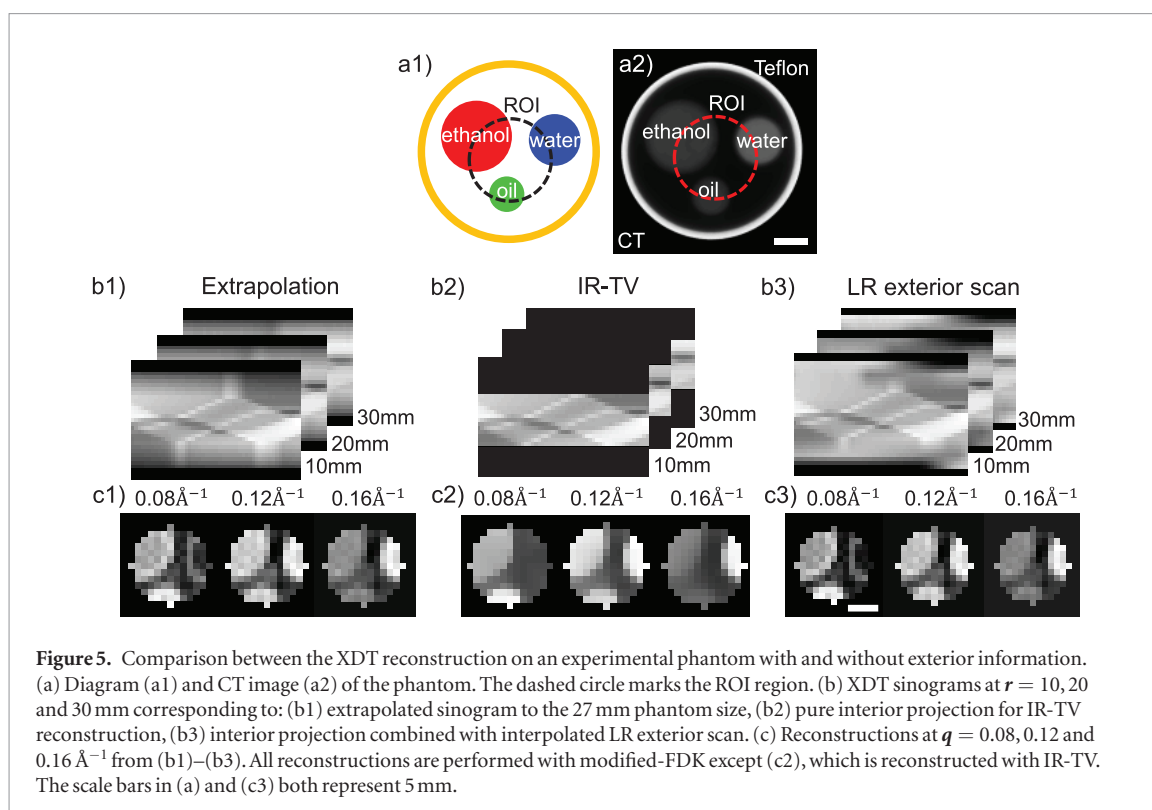
4. Results and discussion

4.1. Simulation results

We first reconstructed the ROI region without additional exterior information. Figures 4(a) and (b) show the measurement and reconstruction from IR-TV and sinogram extrapolation, respectively. In IR-TV, the reconstruction was performed directly on the truncated sinogram (figure 4(a1)) using $\mathbf{H}_2$. In sinogram extrapolation, the truncated sinogram is extrapolated to an 18 mm-diameter support, shown in figure 4(b1). The reconstructed spatial profiles at $q = 0.10, 0.14$ and 0.18 Å^{-1} are shown for IR-TV (a2) and sinogram extrapolation (b2). The NMSE between ROI image and ground truth at these momentum transfer values are 1.4%, 2.2% and 1.6%, respectively for IR-TV, 0.84%, 1.1% and 1.2%, respectively for sinogram extrapolation. The overall NMSE within ROI is 2.0% for IR-TV, 2.1% for sinogram extrapolation, for all momentum transfers. Both IR-TV and sinogram extrapolation can suppress the truncation artifacts found in interior reconstructions (figure 3(e)). It is worth noting that for the sinogram extrapolation in (b1), our simulation uses the true support size $a_1(\phi) = -a_2(\phi) = 9$ mm, which corresponds to the size of the Lucite tube. If wrong values for a_1 and a_2 were used, the reconstruction would yield higher NMSE.

Next, we combined the truncated projections with a simulated LR scan at 1.25 mm intervals outside ROI. The exterior projections were linearly interpolated, shown in figure 4(c1), to match the sampling interval of the ROI. Figure 4(c2) shows the reconstructed spatial profiles at $q = 0.10, 0.14$ and 0.18 Å^{-1}. The NMSE between ROI image and ground truth are 0.36%, 1.2% and 0.66%, respectively. The overall NMSE of the ROI reconstruction is reduced to 1.1%, almost half of the overall NMSE without exterior sampling. Figures 4(d1)–(d3) plot the reconstructed image profile along the red, dashed line at $q = 0.10, 0.14$ and 0.18 Å^{-1}, respectively. For comparison, we also plot the true profiles in figure 4(d). Compared with IR-TV and sinogram extrapolation, LR exterior scan demonstrates the potential to simultaneously preserve spatial features and reduce the artifact, without knowing the support size. We speculate that the poor contrast between Nylon and the surrounding fat region at $q = 0.14$ Å^{-1} (figure 4(d2)) is due to the blurring with the 0.13 Å^{-1} XRD peak of Nylon. This blurring, arising from the tilted projection in the z-q plane, is consistent with the CT cone-beam artifacts, which introduce shading and streaking to the volume near a high-density region (Hsieh 2000).
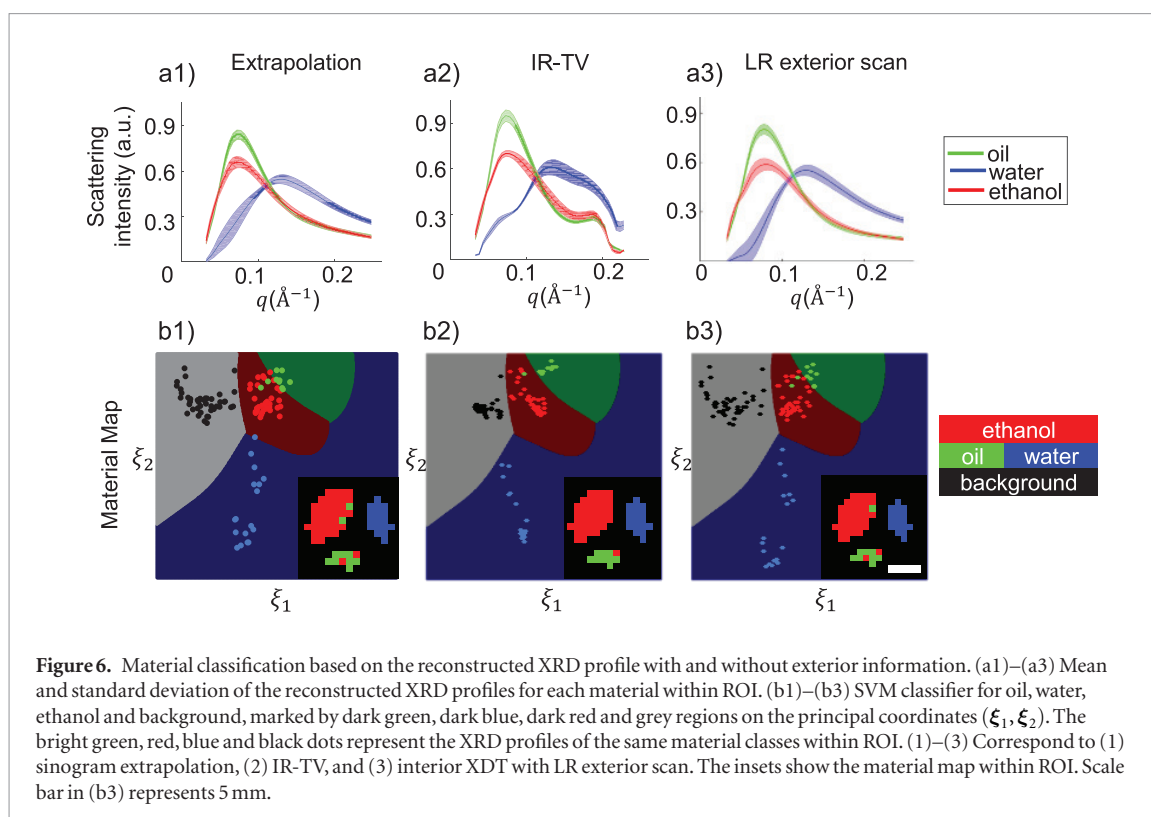
4.2. Experiment results

The structural diagram and the CT image of the phantom analyzed by our system are shown in figures 5(a1) and (a2). The dashed circle marks the ROI region for the interior XDT scan. On the CT image (figure 5(a2)), the

Figure 5. Comparison between the XDT reconstruction on an experimental phantom with and without exterior information. (a) Diagram (a1) and CT image (a2) of the phantom. The dashed circle marks the ROI region. (b) XDT sinograms at $r = 10, 20$ and 30 mm corresponding to: (b1) extrapolated sinogram to the 27 mm phantom size, (b2) pure interior projection for IR-TV reconstruction, (b3) interior projection combined with interpolated LR exterior scan. (c) Reconstructions at $q = 0.08, 0.12$ and $0.16\,\text{Å}^{-1}$ from (b1)–(b3). All reconstructions are performed with modified-FDK except (c2), which is reconstructed with IR-TV. The scale bars in (a) and (c3) both represent 5 mm.

average grayscale value (normalized to maximum) within oil and ethanol regions are 0.17 ± 0.03 and 0.19 ± 0.03, respectively. The contrast between these two materials is comparable with the fluctuation in the reconstructed image, which renders them indistinguishable on CT. XDT reconstructions (figures 5(b) and (c)) were performed using the three ROI reconstruction methods in section 2. The sampling grid for all the reconstructions is 1 mm in the spatial domain, (x, z), and $0.005\,\text{Å}^{-1}$ in the momentum transfer domain, q. The reconstructed ROI regions are displayed at three momentum transfer values $q = 0.8, 0.12$ and $0.16\,\text{Å}^{-1}$. Figures 5(b1)–(b3) show the processed sinograms at $r = 10, 20$ and 30 mm, corresponding to sinogram extrapolation (b1), IR-TV (b2) and LR exterior scan (b3). In figure 5(b1), the truncated sinogram is extrapolated to 27 mm-diameter support, which is the actual size of the phantom. Figures 5(c1) and (c2) show that both IR-TV and sinogram extrapolation to the actual sample size can alleviate the truncation artifact. Due to the use of TV regularization in (c2), ethanol and water contrast less with the surroundings than those in (c1) and (c3), and the plastic vial containing water is invisible in $q = 0.08\,\text{Å}^{-1}$. Figure 5(c3) shows the reconstruction with LR exterior samplings from the interpolated sinogram (b3). The average grayscale at $0.08\,\text{Å}^{-1}$ (normalized to maximum) is 0.91 ± 0.07 within the oil region, and 0.66 ± 0.08 within the ethanol region. The higher intensity of oil at $q = 0.08\,\text{Å}^{-1}$ clearly distinguishes it from methanol, and agrees with its larger molecular form factor (Chantler 1995).

The mean and standard deviation of the reconstructed XRD profiles within water, ethanol and oil regions are plotted in figure 6(a). The primary scattering peaks measured by our system are located at $0.12\,\text{Å}^{-1}$ for water, and $0.077\,\text{Å}^{-1}$ for oil, which are both lower than previous XRD measurements (Kosanetzky *et al* 1987) by a factor of 0.7 due to the beam-hardening effect on the low-energy spectrum, a phenomenon that is also observed in Kidane *et al* (1999) and Zhu and Pang (2018). The XRD profiles reconstructed from LR exterior scan, IR-TV and sinogram extrapolations are compared in (a1)–(a3). To quantify and compare the material specificity among different interior XDT schemes, we performed SVM classifications in figure 6(b). The reference XRD measurements of each material define the boundary of each material classifier, as shown in figures 6(b1)–(b3). For illustration purposes, the XRD profile of every pixel in the ROI is represented by a dot in the 2D space, which is spanned by the first two principal components (ξ_1, ξ_2) obtained from the principal component analysis. The insets in figures 6(b1)–(b4) show the material map of the ROI in each scenario. Among all the pixels in the ROI region, 3.5% (extrapolation), 0.8% (IR-TV), and 2.6% (LR-exterior) are misclassified in (b1)–(b3), respectively. The sinogram extrapolation shows higher classification error than LR exterior scan. In real applications involving irregular-shaped sample, determining the support under every projection angle without additional scan is impossible, which could further increase the classification error in sinogram extrapolation. The TV regularizer, though having high material specificity, could reduce the contrast of high-frequency features in complicated sample structures.

Figure 6. Material classification based on the reconstructed XRD profile with and without exterior information. (a1)–(a3) Mean and standard deviation of the reconstructed XRD profiles for each material within ROI. (b1)–(b3) SVM classifier for oil, water, ethanol and background, marked by dark green, dark blue, dark red and grey regions on the principal coordinates (ξ_1, ξ_2). The bright green, red, blue and black dots represent the XRD profiles of the same material classes within ROI. (1)–(3) Correspond to (1) sinogram extrapolation, (2) IR-TV, and (3) interior XDT with LR exterior scan. The insets show the material map within ROI. Scale bar in (b3) represents 5 mm.

5. Conclusion

In summary, we have demonstrated a quasi-interior XDT system that combines a LR exterior scan to reconstruct the ROI region from limited projection information. We have compared our method with existing interior tomography schemes that rely either on piecewise constant constraints (IR-TV) or knowledge on the support size (sinogram extrapolation) in terms of their reconstructed spatial and scattering profiles in ROI. Although IR-TV, proper sinogram extrapolation and LR exterior scan all suppress the truncation artifacts and provide good material discrimination based on the reconstructed XRD profile, the proposed method preserves the complicated features in the sample, and obviates the knowledge on the size of the object support, thus providing a more general ROI measurement and reconstruction framework for XDT. In addition, the modified-FDK algorithm in our quasi-interior XDT framework is faster and requires less memory than iterative algorithms. Currently the hour-long imaging time is due to the weak XRD signal, and the necessity to overcome the dark noise on the panel detector. The use of photon-counting detector array could further shorten the imaging time to the order of minutes. In the future, we plan to adaptively select the exterior regions based on the ROI location and shape to further reduce unnecessary imaging time and radiation damage. We expect our quasi-interior XDT scheme, combined with photon-counting detectors, to find applications in *ex vivo* biomedical and pathological studies.

Acknowledgment

ORCID iDs

Zheyuan Zhu ⬚ https://orcid.org/0000-0001-9992-135X

References

Bleuet P, Welcomme E, Dooryhée E, Susini J, Hodeau J-L and Walter P 2008 Probing the structure of heterogeneous diluted materials by diffraction tomography *Nat. Mater.* **7** 468–72

Chambolle A 2004 An algorithm for total variation minimization and applications *J. Math. Imaging Vis.* **20** 89–97

Chantler C T 1995 Theoretical form factor, attenuation, and scattering tabulation for $Z = 1$–92 from $E = 1$–10 eV to $E = 0.4$–1.0 MeV *J. Phys. Chem. Ref. Data* **24** 71–643

Cortes C and Vapnik V 1995 Support-vector networks *Mach. Learn.* **20** 273–97

Delfs J and Schlomka J P 2006 Energy-dispersive coherent scatter computed tomography *Appl. Phys. Lett.* **88** 10–13

Feldkamp L A, Davis L C and Kress J W 1984 Practical cone-beam algorithm *J. Opt. Soc. Am.* A **1** 612–9

Harding G 2004 X-ray scatter tomography for explosives detection *Radiat. Phys. Chem.* **71** 869–81

Harding G 2009 X-ray diffraction imaging—a multi-generational perspective *Appl. Radiat. Isot.* **67** 287–95

Harding G L and Schreiber B 1999 Coherent x-ray scatter imaging and its applications in biomedical science and industry *Radiat. Phys. Chem.* **56** 229–45

Harding G, Kosanetzky J and Neitzel U 1987 X-ray-diffraction computed-tomography *Med. Phys.* **14** 515–25

He F *et al* 2017 Multiscale characterization of the mineral phase at skeletal sites of breast cancer metastasis *Proc. Natl Acad. Sci.* **114** 10542–7

Hsieh J 2000 A practical cone beam artifact correction algorithm *2000 IEEE Nuclear Science Symp. Conf. Record (Cat. No. 00CH37149)* vol 2 (IEEE) pp 15/71–4

Jensen T H, Bech M, Bunk O, Thomsen M, Menzel A, Bouchet A, Le Duc G, Feidenhans'l R and Pfeiffer F 2011 Brain tumor imaging using small-angle x-ray scattering tomography *Phys. Med. Biol.* **56** 1717–26

Jin X, Katsevich A, Yu H, Wang G, Li L and Chen Z 2012 Interior tomography with continuous singular value decomposition *IEEE Trans. Med. Imaging* **31** 2108–19

Johns P C and Yaffe M J 1983 Coherent scatter in diagnostic radiology *Med. Phys.* **10** 40–50

Kidane G, Speller R D, Royle G J and Hanby A M 1999 X-ray scatter signatures for normal and neoplastic breast tissues *Phys. Med. Biol.* **44** 1791

Kleuker U, Suortti P, Weyrich W and Spanne P 1998 Feasibility study of x-ray diffraction computed tomography for medical imaging *Phys. Med. Biol.* **43** 2911

Kosanetzky J, Knoerr B, Harding G and Neitzel U 1987 X-ray diffraction measurements of some plastic materials and body tissues *Med. Phys.* **14** 526–32

Kudo H, Courdurier M, Noo F and Defrise M 2007 Tiny *a priori* knowledge solves the interior problem *IEEE Nuclear Science Symp. Conf. Record* vol 6 pp 4068–75

Lavrov S A and Simonov E N 2010 Effect of regrouping of projecting data from fan to parallel geometry in reconstruction of tomographic images *Biomed. Eng.* **44** 114–20

Mochales C, Maerten A, Rack A, Cloetens P, Mueller W D, Zaslansky P and Fleck C 2011 Monoclinic phase transformations of zirconia-based dental prostheses, induced by clinically practised surface manipulations *Acta Biomater.* **7** 2994–3002

Moon T K 1996 The expectation-maximization algorithm *IEEE Signal Process. Mag.* **13** 47–60

Moss R M, Amin A S, Crews C, Purdie C A, Jordan L B, Iacoviello F, Evans A, Speller R D and Vinnicombe S J 2017 Correlation of x-ray diffraction signatures of breast tissue and their histopathological classification *Sci. Rep.* **7** 12998

Natterer F 1986 *The Mathematics of Computerized Tomography* (Philadelphia: SIAM)

Schaff F, Bech M, Zaslansky P, Jud C, Liebi M, Guizar-Sicairos M and Pfeiffer F 2015 Six-dimensional real and reciprocal space small-angle x-ray scattering tomography *Nature* **527** 353–6

Schroer C G, Kuhlmann M, Roth S V, Gehrke R, Stribeck N, Almendarez-Camarillo A and Lengeler B 2006 Mapping the local nanostructure inside a specimen by tomographic small-angle x-ray scattering *Appl. Phys. Lett.* **88** 1–4

Siddon R L 1985 Fast calculation of the exact radiological path for a three-dimensional CT array *Med. Phys.* **12** 252–5

Sottmann J, Di Michiel M, Fjellvåg H, Malavasi L, Margadonna S, Vajeeston P, Vaughan G B M and Wragg D S 2017 Chemical structures of specific sodium ion battery components determined by operando pair distribution function and x-ray diffraction computed tomography *Angew. Chem., Int. Ed. Engl.* **56** 11385–9

Stock S R, De Carlo F and Almer J D 2008 High energy x-ray scattering tomography applied to bone *J. Struct. Biol.* **161** 144–50

Valentini L, Dalconi M C, Parisatto M, Cruciani G and Artioli G 2011 Towards three-dimensional quantitative reconstruction of cement microstructure by x-ray diffraction microtomography *J. Appl. Crystallogr.* **44** 272–80

Van Gompel G, Defrise M and Van Dyck D 2006 Elliptical extrapolation of truncated 2D CT projections using Helgason–Ludwig consistency conditions *Proc. SPIE* **6142** 61424B

Van Gompel G, Tisson G, Van Dyck D and Sijbers J 2004 A new algorithm for 2D region of interest tomography *Proc. SPIE* **5370** 2105

Wang G and Yu H 2009 Compressed sensing based interior tomography *Phys. Med. Biol.* **54** 2791

Wang G and Yu H 2013 The meaning of interior tomography *Phys. Med. Biol.* **58** R161

Westmore M S, Fenster A and Cunningham I A 1997 Tomographic imaging of the angular-dependent coherent-scatter cross section *Med. Phys.* **24** 3–10

Xiao X, De Carlo F and Stock S 2007 Practical error estimation in zoom-in and truncated tomography reconstructions *Rev. Sci. Instrum.* **78** 063705

Yang J, Yu H, Jiang M and Wang G 2010 High order total variation minimization for interior tomography *Inverse Problems* **26** 350131–329

Zhu Z and Pang S 2018 Three-dimensional reciprocal space x-ray coherent scattering tomography of two-dimensional object *Med. Phys.* **45** 1654–61

Zhu Z, Katsevich A, Kapadia A J, Greenberg J A and Pang S 2018 X-ray diffraction tomography with limited projection information *Sci. Rep.* **8** 522